A Transient in Surface Motions Dominated by Deep Afterslip Subsequent to a Shallow Supershear Earthquake

The 2018 M_w7.5 Palu Case

Nijholt, N.; Simons, W. J.F.; Efendi, J.; Sarsito, D. A.; Riva, R. E.M.

DOI
10.1029/2020GC009491

Publication date
2021

Document Version
Final published version

Published in
Geochemistry, Geophysics, Geosystems

Citation (APA)
Nijholt, N., Simons, W. J. F., Efendi, J., Sarsito, D. A., & Riva, R. E. M. (2021). A Transient in Surface Motions Dominated by Deep Afterslip Subsequent to a Shallow Supershear Earthquake: The 2018 M_w7.5 Palu Case. *Geochemistry, Geophysics, Geosystems*, *22*(4), Article e2020GC009491. https://doi.org/10.1029/2020GC009491

Geochemistry, Geophysics, Geosystems

RESEARCH ARTICLE
10.1029/2020GC009491

A Transient in Surface Motions Dominated by Deep Afterslip Subsequent to a Shallow Supershear Earthquake: The 2018 M_w7.5 Palu Case

N. Nijholt[1,2], W. J. F. Simons[2], J. Efendi[3], D. A. Sarsito[4], and R. E. M. Riva[1]

[1]Department of Geoscience and Remote Sensing, Faculty of Civil Engineering and Geosciences, Delft University of Technology, Delft, The Netherlands, [2]Department of Space Engineering, Faculty of Aerospace Engineering, Delft University of Technology, Delft, The Netherlands, [3]BIG (Badan Informasi Geospasial/Geospatial Information Agency), Java, Indonesia, [4]Faculty of Earth Sciences and Technology, ITB (Institut Teknologi Bandung/Institute of Technology Bandung), Geodesy Research Group, Bandung, Indonesia

Abstract The 2018 M_w7.5 Palu earthquake is a remarkable strike-slip event due to its nature as a shallow supershear fault rupture across several segments and a destructive tsunami that followed coseismic deformation. GPS offsets in the wake of the 2018 earthquake display a transient in the surface motions of northwest Sulawesi. A Bayesian approach identifies (predominantly aseismic) deep afterslip on and below the coseismic rupture plane as the dominant physical mechanism causing the cumulative, postseismic, surface displacements whereas viscous relaxation of the lower crust and poro-elastic rebound contribute negligibly. We confirm a correlation between shallow supershear rupture and postseismic surface transients with afterslip activity in the zone below an interseismically locked fault plane where the slip rate tapers from zero to creeping.

Key Points:

- GPS offsets display a postseismic transient throughout NW Sulawesi, Indonesia, in the wake of the 2018 Palu, supershear earthquake
- Deep afterslip below the coseismic fault plane dominates the observed postseismic signal following the 2018 Palu earthquake
- Shallow supershear ruptures correlate with rooted afterslip in the year subsequent to the event

Supporting Information:

- Supporting Information S1

Correspondence to:
N. Nijholt,
n.nijholt-2@tudelft.nl

Citation:
Nijholt, N., Simons, W. J. F., Efendi, J., Sarsito, D. A., & Riva, R. E. M. (2021). A transient in surface motions dominated by deep afterslip subsequent to a shallow supershear earthquake: The 2018 M_w7.5 Palu case. *Geochemistry, Geophysics, Geosystems*, *22*, e2020GC009491. https://doi.org/10.1029/2020GC009491

Received 20 OCT 2020
Accepted 26 FEB 2021

Author Contributions:
Conceptualization: N. Nijholt, W. J. F. Simons, R. E. M. Riva
Data curation: W. J. F. Simons, J. Efendi, D. A. Sarsito
Formal analysis: N. Nijholt, W. J. F. Simons, J. Efendi, D. A. Sarsito
Funding acquisition: W. J. F. Simons, R. E. M. Riva
Investigation: N. Nijholt
Methodology: N. Nijholt, W. J. F. Simons
Project Administration: R. E. M. Riva

1. Introduction

The appearance of transients in the surface deformation field subsequent to a major earthquake is widely recognized in tectonically active regions around the world. The advent of space geodetic techniques has illuminated surface displacement (rates) across spatiotemporal scales. Postseismic deformation signals can be detected above the noise level of interseismic deformation patterns, with postseismic trends lasting from days to decades. A sudden coseismic stress change may be dissipated through (a combination of) several (a)seismic mechanisms: afterslip on the (larger) coseismic fault plane (e.g., Smith & Wyss, 1968), viscoelastic relaxation (flow) of the lower crust and/or upper mantle (e.g., Nur & Mavko, 1974), or poro-elastic rebound due to fluid flow at shallow crustal levels in the vicinity of the coseismic fault plane (e.g., Peltzer et al., 1996). The coseismic slip distribution, nature of surrounding lithologies, and tectonic setting define the extent of the postseismic deformation transients, while the spatial coverage of observations at an earthquake location defines the potential of resolving the mechanisms responsible.

In this study, we focus on deformation associated with the strike-slip Palu-Koro fault (Figure 1a). Quaternary activity of the Palu-Koro fault is denoted in the geomorphology by very narrow, steep valleys as the fault runs through central Sulawesi, Indonesia (Bellier et al., 2001; Katili, 1970; Watkinson & Hall, 2017), and continues offshore where it delimits the western extent of the Minahassa trench (Hamilton, 1979). The Palu-Koro fault is a seismically active fault (Figure 1b) with a multitude of $M_w < 6$ earthquakes; much of the activity at the onshore segment of the Palu-Koro fault (Figure 1c) is detected at shallow levels (Figures 1d and 1e) (Supendi et al., 2020). GPS-derived velocities across the left-lateral Palu-Koro fault (Socquet et al., 2006; Walpersdorf et al., 1998a) indicate that the segment at Palu Bay is locked shallowly, where ~4 cm yr^{-1} of relative plate motion is accommodated (Bellier et al., 2001; Socquet et al., 2006; Walpersdorf et al., 1998b). Combining this geodetic and geomorphological evidence with the attribution of three earthquakes/tsunamis over the past century to Palu-Koro fault activity (Katili, 1970; Prasetya et al., 2001) gives notion to high seismic hazard (Cipta et al., 2017). This notion was confirmed at September 28, 2018, marked by a M_w7.5 supershear earthquake (Bao et al., 2019) that ruptured a ~150 km segment of the Palu-Koro fault system in the vicinity of Palu Bay (e.g., Simons et al., 2018; Socquet et al., 2019). Unexpectedly, the (mostly) shallow slip triggered a tsunami that destroyed a large portion of the Palu Bay coastline (GEER-team, 2019). As a direct consequence of the earthquake, and the induced tsunami, mud flows, and liquefaction, 4,340

Resources: W. J. F. Simons, R. E. M. Riva
Software: N. Nijholt, W. J. F. Simons
Supervision: R. E. M. Riva
Validation: N. Nijholt, W. J. F. Simons
Visualization: N. Nijholt
Writing – original draft: N. Nijholt, W. J. F. Simons
Writing – review & editing: N. Nijholt, W. J. F. Simons, R. E. M. Riva

people lost their lives (GEER-team, 2019). In addition to the destructive coseismic surface motions, postseismic transients are envisaged to shape the coastal areas of northern Sulawesi in the (near) future.

Supershear earthquakes, for which the coseismic rupture speed exceeds the *S*-wave velocity, typically occur on smoothly linear strike-slip faults and are characterized by slip at shallow levels (Reilinger et al., 2000; Wright et al., 2004; Yue et al., 2013). The (early) postseismic transients recorded for the 1999 Izmit and Düzce (Bürgmann et al., 2002; Hearn et al., 2002, 2009; L. Wang et al., 2009), 2002 Denali (Biggs et al., 2009; Freed et al., 2006; Johnson et al., 2009), and 2013 Craig (Ding et al., 2015) supershear earthquakes indicate a distinct presence of deep afterslip on the (shallowly) ruptured fault plane within the first year after the event. Bouchon and Karabulut (2008) note a relative quiescence in aftershocks on the main fault plane of supershear earthquakes, which suggests complete stress release on the main fault interface. The Palu earthquake represents an "atypical" supershear rupture as the rupture jumped across several segments (Figure 2a). With most aftershock activity concentrated near the rupture tips, and some along the eastern

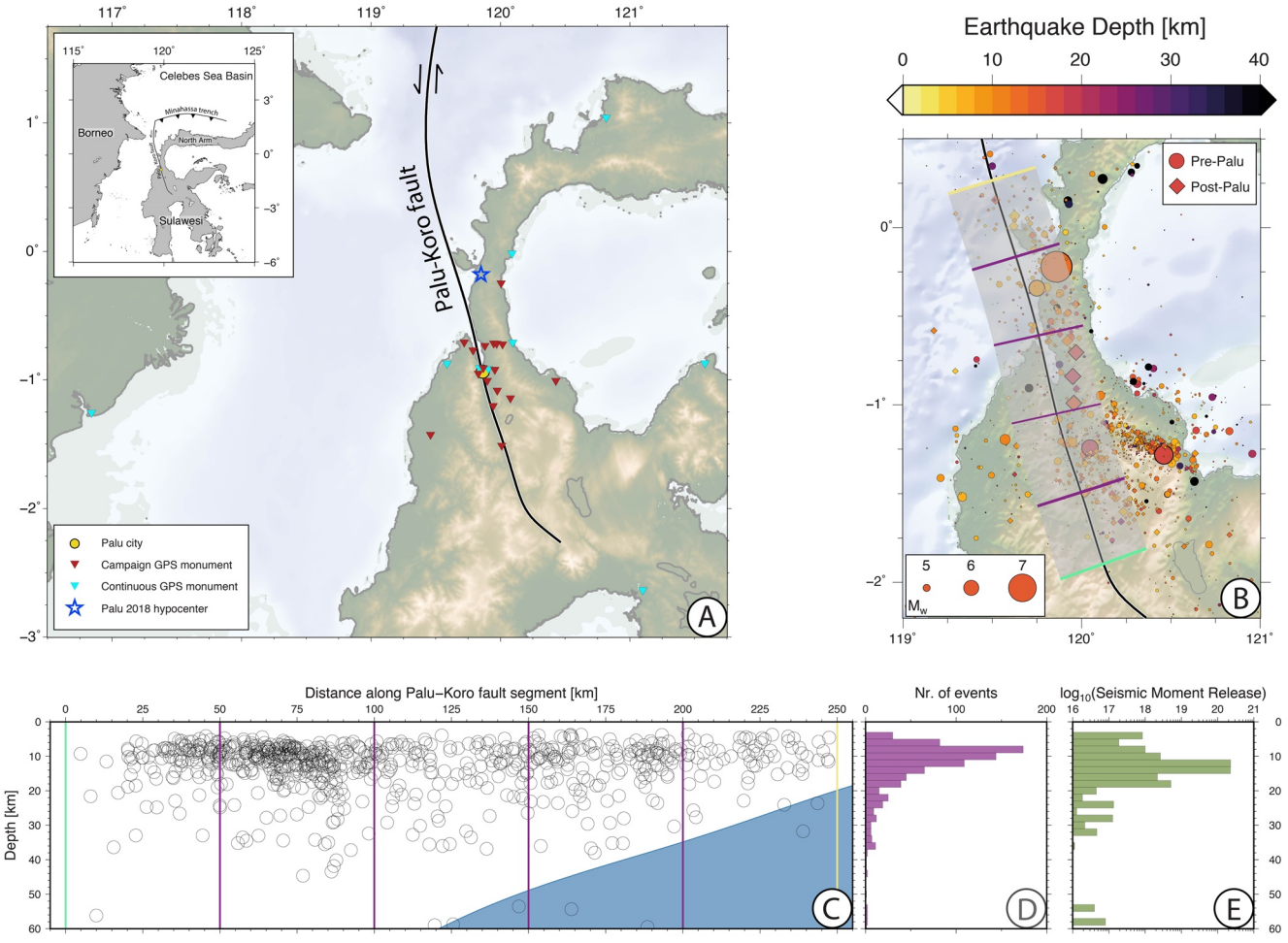

Figure 1. (a) Tectonic setting of the Sulawesi region. Red and light blue triangles indicate the locations of GPS monuments for which the postseismic transient displacements were determined. (b) Map of relocated seismicity ($M_w > 3$) in the onshore region of the Palu-Koro fault 2009–2019 (Supendi et al., 2020), where colored circles indicate depth of the events. Earthquakes recorded before the 2018 M_w7.5 Palu earthquake are noted by circles (pre-Palu), whereas earthquakes that occurred since are denoted by diamonds (post-Palu). Every event within 25 km from the Palu-Koro fault (transparent swath) is mapped onto (c). (c) Vertical cross-section of the seismic activity mapped onto the Palu-Koro fault. Blue plane indicates the presence of the Celebes Sea oceanic crust subjected underneath the North Arm. (d) Histogram of the number of seismic events per 2-km depth bin. (e) Histogram of cumulative seismic moment released per 2-km depth bin. Note, here, that seismologically inferred energy release may not coincide with geodetically inferred energy release, a matter which is relevant only for the larger magnitude events. For example, the M_w7.5 Palu earthquake has "released" its energy at a hypocenter depth of 13 km based on the earthquake focal mechanisms, while most of the coseismic slip is projected onto shallower depths based on surface displacements (e.g., Simons et al., 2018; Socquet et al., 2019; Figure 2a).

flank (Figure 2b), seismic moment release returned to a background level within a couple of days (Supendi et al., 2020; Figure 2c). The question remains which physical mechanism is responsible for postseismic surface transients.

We present postseismic surface displacements accumulated over the year subsequent to the 2018 M_w 7.5 Palu earthquake recorded across the northern Sulawesi region. Through a Bayesian approach, which allows for a probabilistic distribution of relevant model parameters, we seek to identify the causal, physical mechanism responsible for the observed surface transients.

2. Methods

2.1. Global Positioning System (GPS) Offsets From 325 Days of Postseismic Motion

2.1.1. Available GPS Data

We mainly make use of a geodetic GPS campaign network suitable for yielding high precision position results in Central Sulawesi, Indonesia that dates back to the Geodynamics of South and Southeast Asia (GEODYSSEA) 1994–1998 project (Wilson et al., 1998). Since then, this GPS network has been gradually densified to ~ 30 GPS points and yearly remeasured by Delft University of Technology/École Normale Supérieure in cooperation with the Indonesian Badan Informasi Geospasial (BIG) and Institut Teknologi Bandung (ITB). This is to monitor the behavior of the Palu-Koro fault in and around the city of Palu in Central Sulawesi, whereby also four CGPS stations (2000-present) were installed along a transect of the Palu-Koro fault (Socquet et al., 2006). From 2012 onwards, BIG also expanded its national InaCORS GNSS network in other parts of Sulawesi with seven stations.

Before, during and after the 2018 M_w 7.5 earthquake all CGPS stations near the Palu-Koro fault were operational. Many of the GPS points were surveyed less than a year earlier in campaign style. We resurveyed all available GPS points (35) in October/November 2018 for at least three full days to estimate the coseismic displacements. We resurveyed 18 GPS points in August 2019 (for four full days) to assess the postseismic displacements.

2.1.2. GPS Data Processing

The (2002–2019) dual frequency GPS data set (from continuous and campaign observations) has been processed using the scientific GIPSY-OASIS II software version 6.4 (Jet Propulsion Laboratory, 2017). We use the (postprocessing) PPP method (Zumberge et al., 1997) to derive precise daily coordinate results from GPS in the global reference frame solution of the International GNSS Service (IGS14) (Rebischung & Schmid, 2016). Precise ephemeris of GPS satellites along with Earth rotation parameters (nonfiducial style) in IGS14 were obtained from JPL. This enables consistent derivation of highly accurate daily geocentric GPS position time series throughout the entire analyzed time period.

2.1.3. Daily Solutions

We decimated the GPS data (from Receiver INdependent Exchange format (RINEX) ASCII files) to 5-min intervals. The used GPS receiver and antenna types, as well as the (verified) antenna height, were taken from the RINEX files. Then we processed the data zero-differenced into daily coordinates, making use of the ionospheric free combination of the observables with a satellite elevation mask angle of 7°. To take into account the systematic errors of different elevation and azimuth angle of the observed satellites, we applied the IGS14 absolute antenna phase center corrections that were downloaded along with the weekly JPL orbits and clock products. We selected the Vienna Mapping Functions (VMF1) tropospheric mapping function (in estimating both zenith delay and gradients) based on numerical data obtained from actual weather conditions, which are updated daily at the Global Geodetic Observing System website (http://vmf.geo.tuwien.ac.at/). We applied the FES2014b global ocean tide model for which we retrieved the ocean loading from the Onsala Space Observatory website (Bos & Scherneck, 2014). To enhance the coordinate solutions in mainly the east-west direction in this regional area, we resolved the phase cycle ambiguity for each station (Bertiger et al., 2010). Hereby, we used our own daily regional network to simultaneously solve all the phase ambiguities. In a final step, we applied daily transformation parameters to the nonfiducial position solutions, which align the solutions with the IGS14 on each day. These transformation parameters are also

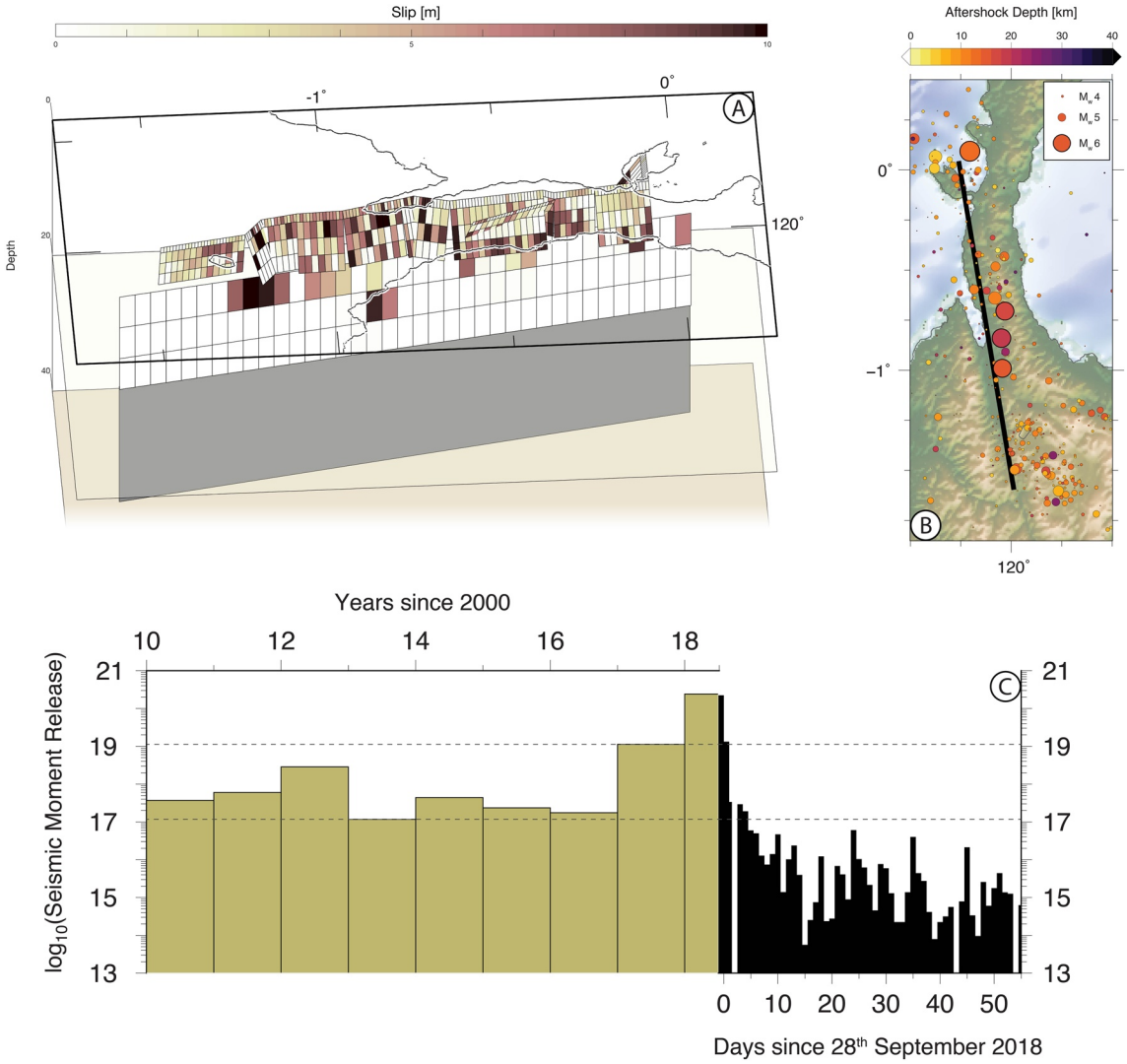

Figure 2. (a) Perspective view of the finite fault model of the M_w7.5 Palu earthquake (Shen et al. (2021), expanding on Simons et al. (2018)). The complex shallow structure extends to a depth of 7 km, whereas the 185-km long deep segment continues to a depth of 22 km. For the afterslip calculations, we extend the bottom segment down to 37-km depth. (b) Map of aftershocks over the ensuing 55 days. Black line indicates "surface trace" of the deep segment of the finite fault. (c) Cumulative seismic moment released in NW Sulawesi over 12-month bins from January 2010 to November 2018 (gold; top axis) and in the days after the 2018 M_w7.5 Palu event (black; bottom axis). Note that the cumulative seismic moment released over a year is heavily dominated by a single event (i.e., the largest that occurred that year; e.g., an M_w6.3 in 2012 and an M_w6.6 in 2017, whereas the largest magnitude in 2014 was an M_w5.3).

provided by JPL and are referred to as X-files. This global reference frame transformation technique delivers the same level of accuracy as the traditional mapping technique whereby GPS data of a subnetwork of IGS steering stations are included in the data analysis (e.g., Mustafar et al., 2017).

2.1.4. Postseismic Displacements

For the 18 reobserved campaign points in 2019, the GPS position time series prior to the earthquake event (i.e., from 2002 to 2018) were used to estimate their velocity trends using linear regression. Earlier coseismic jumps were removed from the data set, that is, at 2005 (M_w6.3 SE of Palu), 2008 (M_w7.4 at the Minahassa trench), 2012 (M_w6.3 SSE of Palu), and 2017 (M_w6.6 SE of Palu, near Poso). Additionally, some campaign position outliers were removed from the GPS time series. The majority of the GPS points were (re)observed using a fixed (screw type) antenna setup to minimize height errors. Thereby also the same GPS antenna type (even with the same serial number at many sites) and GPS receiver types have been used. Only some older points (3) were surveyed using tripods. None of the GPS points were damaged by the earthquake and none are

Table 1
Cumulative Postseismic Displacements After 325 Days in mm

Site	Longitude	Latitude	East	North	Up	σ_{East}	σ_{North}	σ_{Up}
TOBP	120.0950	−0.7090	−12.0000	76.5000	−25.1000	2.8808	3.0131	8.4916
PALP	119.9060	−0.9160	−7.9000	−8.5000	−23.6000	2.2512	1.4682	9.8160
P14P	119.8370	−0.9060	87.7000	−68.6000	−89.9000	7.3175	3.0877	20.6372
WATP	119.5870	−0.8740	8.7000	−35.8000	−14.9000	2.9096	2.4604	12.7885
SNEY	120.0890	−0.0160	10.0000	61.2000	−8.8000	2.3504	3.8897	10.8749
CTOL	120.8170	1.0420	18.8000	28.0000	18.5000	3.4665	3.1635	16.7314
CMLI	121.1000	−2.6340	−1.3000	4.5000	−9.1000	2.9927	1.6184	12.5651
CAMP	121.5800	−0.8710	−3.2000	8.6000	−1.3000	2.2461	1.7618	10.2326
CBAL	116.8400	−1.2560	−0.6000	1.3000	−6.3000	2.1153	1.7904	8.0162
BALA	119.8290	−0.9510	12.6000	−28.9000	−28.5000	2.1260	0.8602	7.7820
BARA	119.4600	−1.4270	−9.4000	−30.0000	−3.1000	5.6400	4.0497	11.1140
DONG	120.0050	−0.2480	1.4000	48.5000	9.1000	1.5000	1.4866	9.7509
KRPU	119.9480	−0.7160	−6.4000	42.7000	0.3000	7.2250	2.4083	13.5949
LOLI	119.7880	−0.7700	17.7000	−24.6000	22.4000	4.8010	2.3431	10.5005
PL04	119.7200	−0.7080	14.5000	−35.2000	−10.8000	6.0141	6.2201	9.8270
PL10	119.8800	−0.7350	6.3000	12.6000	−31.0000	7.8517	5.3075	11.9403
PL18	119.8670	−0.9080	−6.1000	−54.2000	−16.9000	2.5632	2.1840	9.3477
PL19	119.9710	−0.7180	−11.4000	53.7000	−50.5000	7.3756	3.0414	16.6400
PL20	119.9560	−0.9210	−12.6000	37.3000	5.5000	4.3566	3.1765	11.1732
PNDE	119.9440	−1.2030	−52.8000	28.4000	−46.1000	6.5069	3.8079	14.7733
PTYA	119.8980	−1.0070	−3.7000	−16.9000	−36.8000	14.6649	5.6400	21.6086
SGPU	119.9750	−1.0830	−7.9000	46.9000	41.6000	2.2803	1.1402	12.5228
SLBY	120.0160	−0.7230	4.5000	46.9000	−9.3000	2.2472	2.5807	11.1041
SULI	120.4280	−1.0070	−9.7000	27.4000	−29.0000	2.1932	2.2803	14.8219
SUNG	120.0100	−1.5120	−21.1000	3.0000	17.8000	3.9825	2.1932	8.9872
THRP	120.0770	−1.1430	−14.9000	50.2000	−27.9000	2.7459	1.9799	9.2099

located directly in areas that suffered from soil liquefaction. The root mean square (RMS) of the (prequake) campaign position differences with respect to their linear trend estimates is 3.3, 3.1, and 9.5 mm in the north, east, and vertical directions, respectively. The 2019 GPS remeasurement campaign resulted in coordinate repeatabilities (weighted RMS) of 1.3, 1.2, and 6.6 mm in the north, east, and vertical directions, respectively.

GPS data were analyzed in an identical way for the eight continuous stations. We obtain linear velocities predating the 2018 M_w7.5 earthquake (based on a 3-year time period (2016–2018)) whereby also (vertical) seasonal variations based on Blewitt and Lavallée (2002) were estimated. These linear velocity estimates are then removed from the postquake daily position solutions (RMS of 1.2, 1.4, and 4.9 mm in the north, east, and vertical directions, respectively) over the 3-week duration of the 2019 GPS campaign. We list the interseismic velocities for campaign and continuous GPS monuments in Table S1, and display them in Figure S1.

The postseismic displacements listed in Table 1 result from removing both the (long-term) (2002–2018) interseismic velocities and instantaneous coseismic displacements from the GPS position time series. Simons et al. (2018) determined the coseismic displacements (resulting from the same GPS data analysis). Accumulated postseismic displacements of Table 1 are displayed as the red arrows in Figures 4–6. The final standard deviations (σ) of the postseismic displacements are based on the coordinate repeatabilities (weighted RMS) of the postquake campaign remeasurements, the extrapolated σ of the interseismic velocity estimates (multiplied by the time passed since the last preearthquake observations) and the σ of the coseismic estimates.

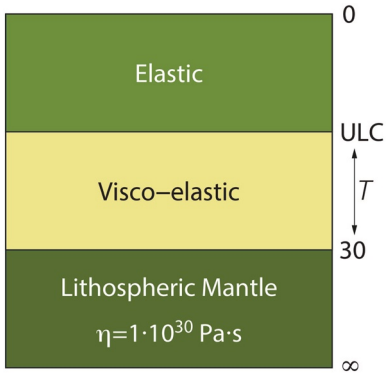

Figure 3. Model setup for the forward calculation of lower-crustal flow: an elastic upper crust overlays a viscoelastic lower crust of thickness T (between the upper-lower crust (ULC) transition and the Moho at 30 km. The lower crust overlays an infinite half-space of high-viscosity, resembling a strong lithospheric mantle.

2.2. Representation of Physical Mechanisms

It is our aim to find the physical mechanism responsible for the observed postseismic transients in the wake of the 2018 M_w 7.5 Palu earthquake. We consider three candidate mechanisms, which we treat individually through forward models: viscoelastic relaxation of the lower crust, afterslip on the (larger) fault plane, and poro-elastic rebound.

We drive viscoelastic relaxation using the coseismic stress change generated through a finite fault model (Figure 2a). This robust finite fault solution (Shen et al. (2021), following Simons et al. [2018]) was determined through a Bayesian inversion of an extensive geodetic data set incorporating coseismic GPS offsets, Satellite Aperture Radar (SAR) pixel offsets, SAR interferometry (InSAR) and Multiple Aperture InSAR (MAI). In order to compare forward model results with postseismic GPS offsets, we compute the resultant surface displacements after 325 days using the PSGRN/PSCMP software (R. Wang et al., 2006). With the shallow nature of the Palu fault rupture in mind, we focus on lower-crustal flow; as depicted in Figure 3, we employ a lower crust of variable thickness (range 5–15 km) and with a variable Maxwell viscosity η (range 1×10^{17}–1×10^{22} $Pa\ s$). The minimum depth of the upper-lower crust transition (ULC in Figure 3) coincides approximately with the downward extent of aftershock activity (Supendi et al., 2020). The lower-crustal layer is overlain by an elastic (upper crustal) layer and underlain by a high-viscosity (1×10^{30} Pa s) half-space, which resembles a strong lithospheric mantle (in the supporting information we test the effect of including a viscoelastic upper mantle). The Moho is set at a depth of 30 km. In order to search the parameter space efficiently, we precalculate forward model solutions on a 0.02 interval (0.02 km for the lower-crustal layer thickness and 0.02 increments for the value of the $log_{10}(\eta)$).

We model cumulative afterslip through the Okada (1992) formulations of a series of buried dislocations in an elastic half-space), using a shear modulus of 32×10^9 Pa. In order to retain a simple geometry, and in line with Stevens et al. (1999) and Socquet et al. (2006), we do not include the uppermost series of variably oriented segments (Figure 2a) and increase the depth of the bottom segment of the coseismic finite fault model to extend between 7 and 37 km. We divide this larger fault into 10 equal-size patches of 37 ×15 km. Any increase in resolution appears unnecessary as we only have a limited set of GPS monuments to compare model predictions with. An increase in fault patch resolution would then require a self-imposed regularization (or smoothing), a redundant operation in a Bayesian search method (Duputel et al., 2014; Minson et al., 2013). The slip magnitude and rake of each potential slip patch are variable and range between 0 and 5 m and between ±45° from pure left-lateral slip, respectively.

Poro-elastic rebound results from pore-fluid flow at shallow crustal layers due to induced coseismic stress changes. Surface deformation thus changes while the medium transitions from an undrained (coseismic) to a drained (sometimes after the earthquake) as pore-fluid pressure reaches a new equilibrium (e.g., Peltzer et al., 1996). The effect does not reach far from the fault trace (<30 km) and is largest for fault ruptures across multiple segments (Peltzer et al., 1996). In the poro-elastic rebound process, the Bulk modulus of the medium decreases but the shear modulus does not (the medium itself is deemed not to have faulted additionally through that one earthquake) and the Poisson ratio decreases. We set the Poisson ratio of the undrained medium at 0.25, as per the finite fault solution, whereas the drained Poisson ratio remains a variable (range 0.20 – 0.25); we compute the elastic response to the coseismic finite fault solution and subtract the undrained from the drained surface displacements to obtain the poro-elastic rebound.

2.3. Searching the Parameter Space

We seek to constrain the most likely ranges for input parameters. Consider the generic formulation of a linear forward problem $\bar{d}_{obs} = G\bar{m}_{inp}$, where $\bar{d}_{obs}$ is the vector constituted by all of the observed quantities (data), $\bar{m}_{inp}$ is the vector constituted by all of the forward model input parameters, and G is a Green's func-

tion matrix which translates input model parameters to quantities $G\bar{m}_{\text{inp}}$ that are subsequently compared to observations. In a linear inverse problem, the difference between the observations $\bar{d}_{\text{obs}}$ and model predictions $G\bar{m}_{\text{inp}}$ is minimized

$$\left(\bar{d}_{\text{obs}} - G\bar{m}_{\text{inp}}\right)^T C^{-1}\left(\bar{d}_{\text{obs}} - G\bar{m}_{\text{inp}}\right),$$

where C is an error-covariance matrix. This includes measurement uncertainties, but the forward model itself also introduces errors (i.e., forward calculations are performed for idealized/simplified mediums and/or geometries). However, a linear inversion will not constrain likely ranges for input parameters.

We therefore take a Bayesian approach to robustly constrain relevant model input parameters and identify parameter trade-offs through calculating probability distributions. Bayes' theorem (Tarantola, 2005) states that the posterior probability distribution $P(\bar{m}_{\text{inp}}|\bar{d}_{\text{obs}})$ is proportional to the likelihood of observing the data given the model $P(\bar{d}_{\text{obs}}|\bar{m}_{\text{inp}})$ and any prior information on the input model parameters $P\left(\bar{m}_{\text{inp}}\right)$

$$P(\bar{m}_{\text{inp}}|\bar{d}_{\text{obs}}) \propto P\left(\bar{m}_{\text{inp}}\right)P(\bar{d}_{\text{obs}}|\bar{m}_{\text{inp}}).$$

We use the Metropolis-Hastings algorithm (following Herman and Govers (2020)) to sample from the posterior probability distribution as we search the parameter space. A resultant, large ensemble of models provides a distribution of plausible model input parameters given the data; we combine the results of several, separate, randomly initialized search chains, after disregarding the first 50,000 iterations per chain that we treat as burn-in. The results from this ensemble produce parameter means, uncertainties, and covariances. We do not have any, reliable prior information on model input parameters, so we set the prior probability distributions wide and uniform: probability equals 1 when within the range and 0 when outside the range. Assuming Gaussian uncertainties, the posterior probability distribution can be written proportional to the likelihood as

$$P(\bar{m}_{\text{inp}} \mid \bar{d}_{\text{obs}}) \propto \frac{1}{(2\pi)^{N/2}\left|C_B\right|^{1/2}}\exp\left(-\frac{1}{2}\left(\bar{d}_{\text{obs}} - G\bar{m}_{\text{inp}}\right)^T {C_B}^{-1}\left(\bar{d}_{\text{obs}} - G\bar{m}_{\text{inp}}\right)\right),$$

where C_B is an error-covariance matrix and N is the number of observations. For calculation speed, we only consider the diagonal terms of the covariance matrix. C_B consists of a data covariance matrix C_d filled with measurement errors, and a model covariance matrix C_m filled with model prediction errors e_p: $C_B = C_d + C_m$. Model prediction errors are weighted by the magnitude of the observed GPS offsets: $C_B = I \cdot \left(\left(\bar{d}_{\text{obs}} \cdot e_p\right)^2\right)$ (Minson et al., 2013). The relevance of accounting for model prediction errors was demonstrated in previous studies (e.g., Duputel et al., 2014; Minson et al., 2013), and the value of e_p (range $0-1$) is determined through the Bayesian approach. Through the inherently idealized scenario calculated in forward models, errors associated with the model assumptions are typically much larger than the geodetic observation errors. By including model prediction errors, the search will continue to focus on those signals in the data that can be explained by the mechanism imposed by the forward model rather than map it onto the available model parameters solely. With a robust sampling, the posterior probability distribution is proportional to the relative frequency in the ensemble of solutions; hence, we display marginal probability distributions as 1-D and 2-D histograms.

We test the potential to resolve model input values for the postseismic mechanisms singly given the available spatial distribution of GPS monuments (Figures S2–S5). The obtained posterior probability distributions confirm that our search methodology is able to return mean values of model parameters given the available observations for idealized forward models. We test whether we can explain the observed, cumulative postseismic surface motions in the wake of the 2018 M_w7.5 Palu earthquake starting with poro-elastic rebound only. Subsequently, we identify the effect of viscoelastic relaxation of the lower crust and we determine the potential combination of viscoelastic relaxation, poro-elastic rebound, and (deep) afterslip lastly.

3. Results and Analysis

3.1. Poro-Elastic Rebound

Figure 4a depicts the horizontal displacements through poro-elastic rebound using the mean Poisson's ratio displayed in the marginal posterior distribution of Figure 4c. Even though this ensemble of models yields a mean value of statistically well-fitting model parameters, the overall match in terms of both magnitude and azimuth is poor. The surface response to poro-elastic rebound displays vertical components, which have a large magnitude (Figure 4b); for most stations, the observational uncertainty is exceeded. The poor fit with the observations is reflected in the mean model prediction error centered on ~ 0.55 (Figure 4d), suggesting that poro-elastic rebound may have a contribution to the observed postseismic transients but it is unlikely to constitute the main causal mechanism.

3.2. Viscoelastic Relaxation of the Lower Crust

The mean values of input parameters determined through the Bayesian approach result in a prediction of cumulative postseismic motions of lower-crustal flow (blue arrows in Figures 5b and 5c) that match the general trend of the observed displacements (red arrows in Figures 5b and 5c) in terms of magnitude and azimuth. This statistically determined, well-fitting model underestimates the horizontal velocities for the northernmost stations, far from the coseismic rupture. The small magnitude of the resultant vertical displacement generally falls within the large uncertainties of the observations. One dimensional marginal posterior distributions (Figures 5d and 5e) indicate that the thickness of the lower-crustal layer is likely to reach 7.16 ± 1.66 km, that is, within the depth bracket of 22.84–30 km, with a Maxwell viscosity $log_{10}\eta = 17.75 \pm 0.18$ *Pa s*. The 2-D marginal posterior distribution (Figure 5f) highlights that the viscosity of the lower crust is correlated with the thickness of the layer. Figure 5g depicts the model prediction error with the mean value centering on ~ 0.35, which means that another mechanism may play a causal role in the observed postseismic transients.

We use a set of preliminary model results of viscoelastic relaxation to test the potential effect of upper mantle relaxation. Figure S6 summarizes these results. Adding a viscoelastic upper mantle to the model has little effect to the resultant surface deformation in case of a Maxwell viscosity where $\eta > 5 \times 10^{18}$ *Pa s* (we note here that 1×10^{19} *Pa s* is a generic value found in similar tectonic settings around the world (e.g., K. Wang et al., 2012; Wright et al., 2013)). The predicted surface motion pattern when including a generic upper mantle viscosity is only amplified slightly (<10%). The probability of such models is similar as the data fit improves for some stations but deteriorates for others. The surface effect changes for upper mantle viscosity values lower than 5×10^{18} *Pa s* as the far-field component of surface displacements reaches magnitudes comparable to the observations. However, in such case, the near-field is overestimated severely so that the conclusion can only be that the 325 days observation period available indicates that the upper mantle has a viscosity high enough not to contribute significantly to the surface deformation. Therefore, far-field deformation must be caused by a different deformation mechanism.

3.3. A Combination of Lower-Crustal Flow, Poro-Elastic Rebound, and Afterslip

We use a set of preliminary model results of afterslip only to test its potential depth distribution by comparing model predictions for slip between 7 and 22 km (Figure S8), 22 and 37 km (Figure S9), and 7 and 37 km (Figure S10; note that the surface displacements are visually identical to Figure 6). Results show that the smallest model prediction error is determined for a model of afterslip from on a fault plane at 7–37 km. The downward extension of the coseismic fault plane for afterslip is thus constrained by the data.

Because we cannot use stringent constraints on the exact contribution of viscoelastic relaxation or poro-elastic rebound in advance of our Bayesian methodology to infer the causal mechanism underlying the cumulative postseismic surface motions, we combine these two mechanisms with a search for afterslip on the down-dip extended, coseismic fault plane (Figure 2a). Figures 6a and 6b display the map-view comparisons of the horizontal and vertical surface motions predicted by the posterior mean model along with the surface trace of the buried fault patches. The posterior mean slip distribution results in cumulative surface displacements that match most of the near-field stations, with the exception of the station at the southern-

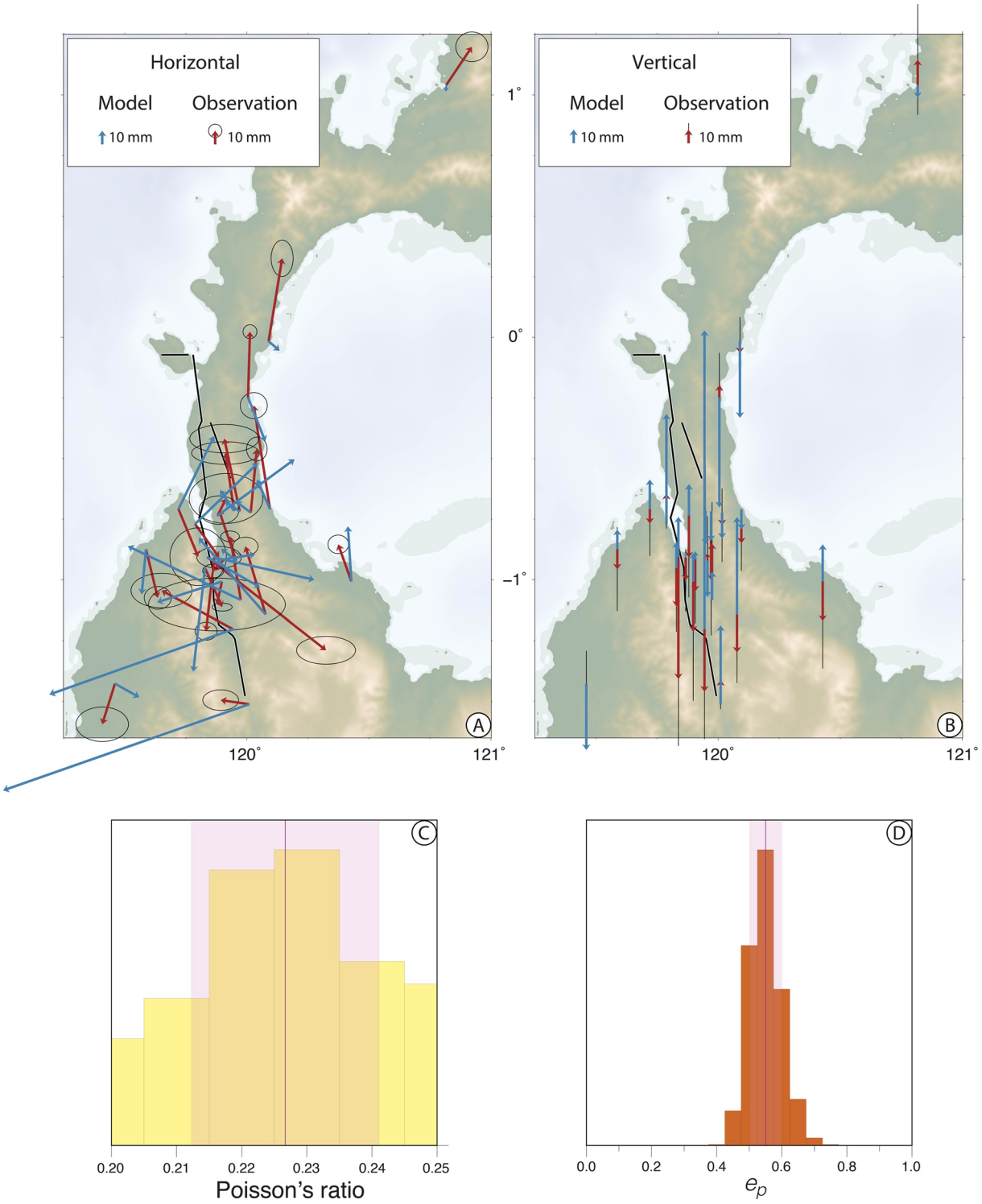

Figure 4. Comparison of the horizontal (a) and vertical vectors (b) of the observations with a model prediction for poro-elastic rebound and the posterior mean value of the Poisson's ratio. Very small arrows are normalized by their magnitude. Black and white lines indicate the surface trace of the coseismic model used. A version of these figures zooming into the Palu Valley and Bay area is available as Figure S11. Panels to the right depict the 1-D marginal probability distributions for the "drained"/postseismic Poisson's ratio (c) and the model prediction error (d). Purple line indicates the mean value of the distribution with the 2-sigma as the transparent swath. Ensemble size is ~200,000.

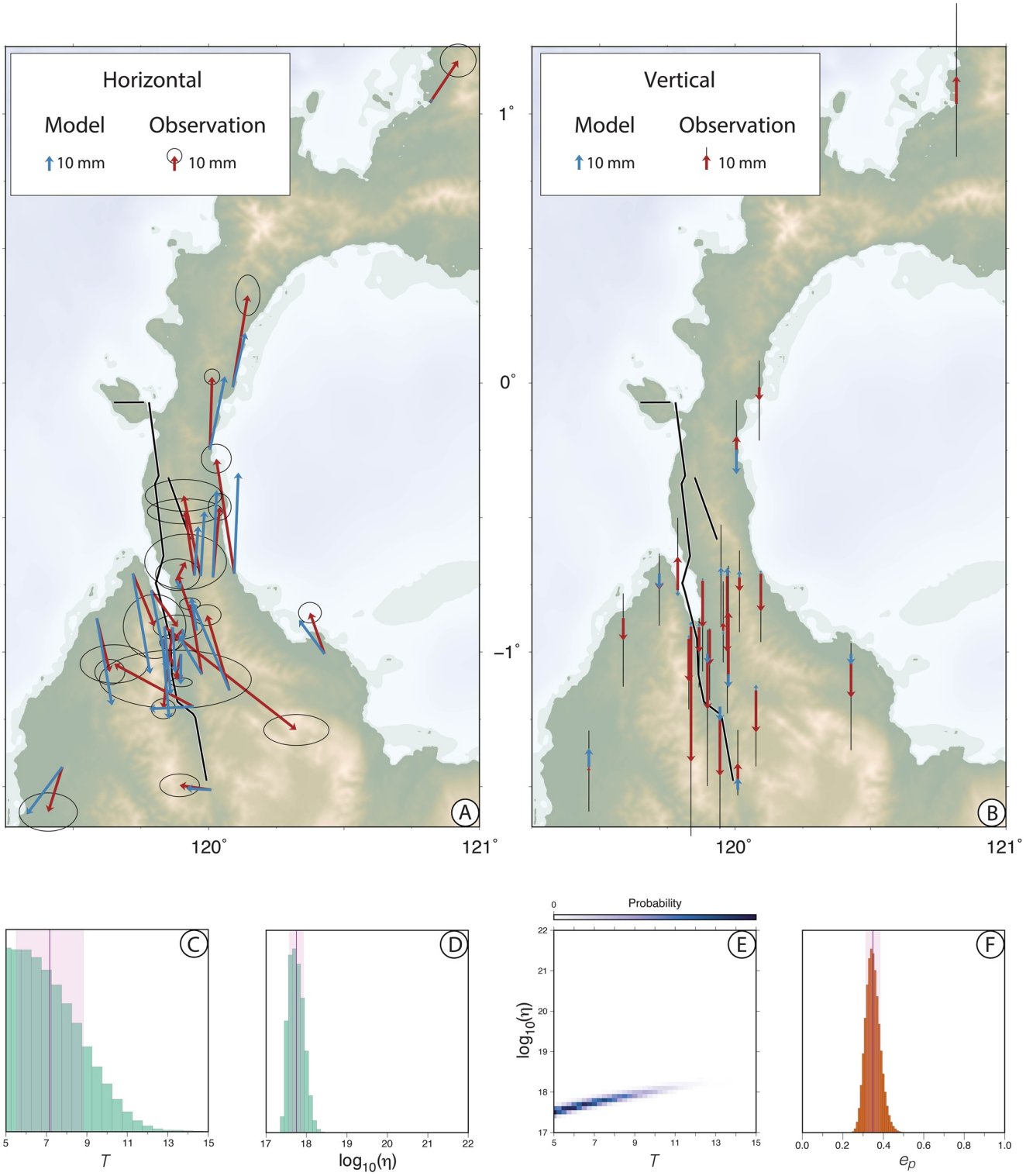

Figure 5. Comparison of the horizontal (a) and vertical (b) vectors of the cumulative, postseismic GPS offsets (red) and model predictions (blue) based on the mean value of the posterior distributions of the layer thickness and viscosity. Very small arrows are normalized by their magnitude. A version of these figures zooming into the Palu Valley and Bay area is available as Figure S12. The bottom row of panels depicts the 1-D marginal probability distribution for the thickness (c) and viscosity (d) of the lower-crustal layer, the 2-D marginal probability distribution of the thickness and viscosity of the lower-crustal layer (e), and the model prediction error (f). Purple line indicates the mean value of the distribution with the 2-sigma as the transparent swath. The ensemble size is ~ 6 million.

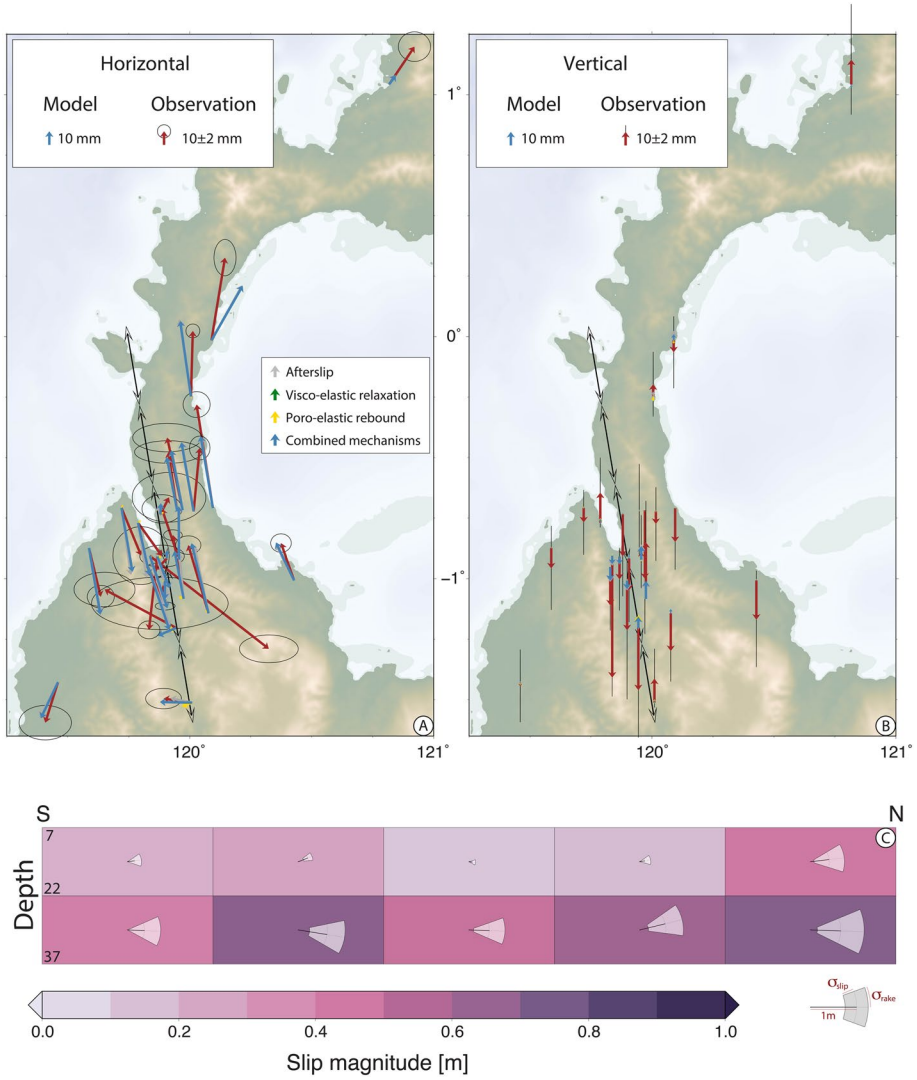

Figure 6. Comparison of the horizontal (a) and vertical vectors (b) of the observations with the posterior mean values of the forward models in the combined search of viscoelastic relaxation, poro-elastic rebound, and afterslip. Very small arrows are normalized by their magnitude. Double-headed arrows indicate the surface trace extent of the fault patches used for the afterslip. A version of these figures zooming into the Palu Valley and Bay area is available as Figure S13, with station names. (c) Finite fault representation of the inferred mean, deep afterslip on the Palu-Koro fault plane given the observed GPS offsets (red in a and b). The gray swaths in the slip and rake direction indicate their 2-sigma bounds. The ensemble size is ~ 5.5 million.

most kink of the coseismic fault model (at the southern extent of Palu Valley) and the two stations closest to Palu City (just south of Palu Bay). Predicted displacements at the far-field station on the North Arm equals almost 0 mm, suggesting a different physical cause for the observed, noninterseismic displacement. The mean posterior model does not display large magnitude vertical displacements, the largest of which are very close to the surface trace of the deep segment of the Palu-Koro fault. Figure 6c displays the distribution of afterslip along the deep segment of the Palu-Koro fault, where the largest contribution to the surface motions stems from the deep segments.

The fit to the observations has improved when including afterslip than was obtained for models of viscoelastic relaxation of the lower crust or poro-elastic rebound singly. These two mechanisms have a very small contribution only to the cumulative surface deformation field in our search of coexisting mechanisms. The posterior mean viscosity exceeds 1×10^{20} *Pa s* (Figure 7a), without strong constraints on the lower-crustal layer thickness. As the predicted surface motion through lower-crustal flow reaches the magnitudes of the

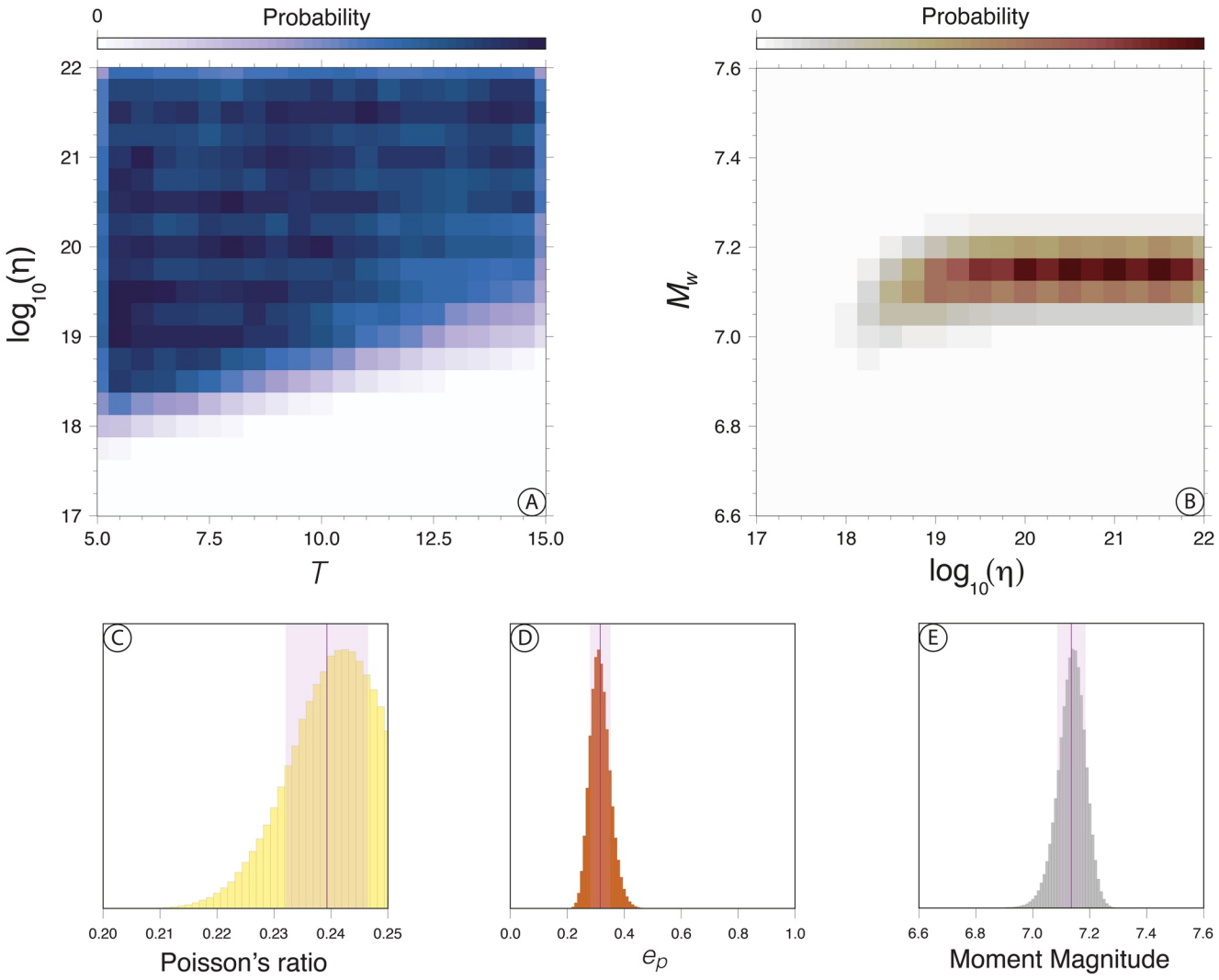

Figure 7. Probabilities for the combined model illustrated in Figure 6. (a) 2-D marginal probability for the thickness and viscosity of the lower-crustal layer. (b) 2-D marginal probability for the viscosity of the lower-crustal layer and the moment magnitude of afterslip. The bottom row of panels includes 1-D marginal probability distributions of the "drained" Poisson's ratio (c), the model prediction error (d), and moment magnitude released through afterslip (e). Purple line indicates the mean value of the distribution with the 2-sigma as the transparent swath.

observational error margins when above 1×10^{19} *Pa s*, it thus appears that this mechanism is statistically irrelevant given the data available. Figure 7b illustrates that lower magnitude viscosity values display a trade-off with afterslip, whereas the most likely model predictions are found for those models with high magnitude lower-crustal viscosity; afterslip is thus the dominant factor. The poro-elastic rebound effect is also very small, and suggests only a small reduction in the Poisson ratio of ~ 0.01 from the coseismic to the postseismic situation (Figure 7c).

Including afterslip in the inversion process has increased the potential to explain the observations, as the model prediction error has been reduced to ~ 0.31 (Figure 7d), which is almost indistinguishable from model results of afterslip only (Figure S10). The mean total moment released through the mean posterior afterslip equals ~ M_w 7.13 (Figure 7e). The total moment released through afterslip equals ~ 30% of the coseismic moment released, which is in line with many other earthquakes (Wimpenny et al., 2017). The inferred cumulative slip displacements greatly exceed the expected interseismic slip on the Palu-Koro fault of ~35 mm accumulated over these 325 days based on the inferred interseismic slip rate (Socquet et al., 2006). The relatively large error margins for the observed verticals and the dominance of slip on deep patches are likely the cause for a relatively weakly constrained rake at many of the slip patches.

4. Discussion

The extensive set of forward models that constitute the posterior probability distributions in the Bayesian searches presented in this study indicate that deep afterslip is the most prominent mechanism responsible for the cumulative postseismic surface displacements in the wake of the 2018 M_w7.5 Palu supershear earthquake. We attribute the surface deformation to a nonuniform slip distribution on a single segment of the deep Palu-Koro fault system (based on the coseismic rupture and kept deliberately simple) fitting both the near-field and far-field GPS offsets at both sides of the Palu-Koro fault. We note that the interseismic locking depth of the Palu-Koro fault is ~12 km (Socquet et al., 2006; Walpersdorf et al., 1998a), and predominance of earthquake activity in close vicinity of the main strand is located at shallow levels (but extending toward 40 km depth; Figures 1c–1e). Within the interseismic creep framework of a constant stress (Bruhat, 2020; Johnson & Segall, 2004), inferred afterslip activity on our set of slip patches then coincides with the "pseudo-coupled" (Herman et al., 2018) section of a fault where the slip rate tapers down-dip from 0 to its interseismic, freely slipping value. Repeating earthquakes and slow slip events have been identified on other, extensively monitored, continental strike-slip faults in this same depth range (Rousset et al., 2019; Uchida et al., 2019). The cumulative nature of the GPS offsets does not allow us to identify spatiotemporal deviations in the postseismic trend (Bacques et al., 2018, 2020) as deep afterslip feasibly causes the surface deformation. The equivalent seismic moment released through the (apparently mostly aseismic; Figures 2b and 2c) afterslip in the mean posterior model equals ~ M_w7.13, and is smaller than the coseismic rupture but much larger than its interseismic value over this time period.

The large majority of observation points in the near-field are campaign measurements. Whereas a number of continuous stations are present in the area, most of the far-field stations have not recorded a large magnitude deviation from their interseismic trend. Local effects in the Palu Valley feasibly affect the observed postseismic motions there, as the two stations near Palu City display a trend not shared within the wider distribution of campaign measurements (the two stations just south of Palu Bay), potentially due to adjacent landslide activity (Watkinson & Hall, 2019). This leaves only two continuous stations within ~50 km of Palu City, and thus not a significant spatial distribution to compare forward models of lower-crustal, viscoelastic relaxation to, noting that the shallow nature of the supershear rupture motivated the inclusion of lower-crustal viscous relaxation. Future observations of postseismic surface motions are likely to put constraints on the potential contribution that viscous relaxation of deeper crustal, or lithospheric mantle, layers makes to surface motions; the cumulative displacements distributed across northern Sulawesi presented in this study do not provide a temporal signal whereby decay constants used in forward models of relaxation of Burgers or power-law materials can be constrained. In this, we consider it not unlikely that viscous relaxation does provide a background signal not forwarded in our combined Bayesian inversion; it will require a strong temporal and spatial signal over a longer time frame than the 325 days of this study to put constraints on such material parameters. Any residuals can then still be the result of afterslip on the fault plane.

Whereas deep afterslip provides a statistical explanation for the majority of the postseismic displacements presented, it is not necessarily the case that this process has been active throughout most of the 325 days nor is it likely that it will continue far into the future as most of the coseismic stress changes have been dissipated. Our inference of afterslip rooting a shallow supershear rupture and dominating surface transients aligns with other studies of postseismic surface transients in the wake of supershear earthquakes; the inferred afterslip falls within a similar depth range, with the largest slip below the coseismic rupture plane (e.g., Freed et al., 2006; Hearn et al., 2009; L. Wang et al., 2009). These studies highlight that viscous relaxation processes provide a key contribution to postseismic transients only months subsequent to the earthquake. We find that surface deformation due to viscoelastic relaxation of the upper mantle does not produce a signal that simultaneously explains both near-field and far-field observations in our time-window satisfactorily. Therefore, even in the presence of a viscoelastic upper mantle, the Bayesian search approach would return similar mean values of lower-crustal viscosity and thickness. Observed far-field motions are thus likely to be caused by a different physical mechanism.

Vigny et al. (2002) report a mechanical interaction between the Minahassa subduction interface and the Palu-Koro fault. In the years following the 1996 M_w7.9 subduction earthquake, the Palu-Koro fault slip rate exceeded its interseismic magnitude (Walpersdorf et al., 1998a). As our Bayesian approach to explain

postseismic displacements in NW Sulawesi subsequent to the 2018 M_w 7.5 Palu earthquake is not able to resolve any significant surface motion at the station on the North Arm, we posit the hypothesis there indeed exists a bilateral mechanical interaction on the scale of the earthquake cycle; the interseismic slip rate on the Minahassa subduction interface is mechanically (but probably temporarily) altered due to the postseismic effects of the strike-slip earthquake, as observed vice versa by Walpersdorf et al. (1998b) and Vigny et al. (2002). Future observations are needed to confirm or refute this hypothesis.

5. Conclusions

GPS offsets in northwestern Sulawesi display cumulative, postseismic, surface displacements in the wake of the 2018 Palu supershear earthquake. These transients are very likely caused by (predominantly aseismic) afterslip on and below the coseismic rupture plane. The mean values and uncertainties of postseismic model input parameters determined through a Bayesian approach in this study indicate that viscous relaxation of the lower crust and poro-elastic rebound contribute negligibly to the cumulative surface displacement transients. The observed coseismic and postseismic characteristics of the 2018 Palu earthquake, in terms of both geodetic and seismological observations, display a correlation between a shallow supershear rupture and surface transients with afterslip activity in the underlying, pseudo-coupled zone of an interseismically locked fault plane.

Conflict of Interest

The authors declare no conflicts of interest relevant to this study.

Data Availability Statement

Processed GPS data and model output files are archived at https://doi.org/10.4121/13537541.v1 in the institutional repository of TU Delft. Seismological data shown in Figures 1 and 2 for this research are included in this paper (and its supporting information files) (Supendi et al., 2020). Software for computing fault slip and surface displacements and performing the search is available online (https://doi.org/10.5281/zenodo.3894137) and we follow the methodology outlined in Herman and Govers (2020). We use the PSGRN/PSCMP software of R. Wang et al. (2006) to compute viscous relaxation, which is available online (https://git.pyrocko.org/pyrocko/fomosto-psgrn-pscmp/). The interseismic GPS velocity estimates (Simons et al., 2018) are included in table format in the supporting information. The GPS data from the (continuous) CORS stations in Indonesia are available (at no cost) from BIG through http://bit.ly/corsBIG.

Acknowledgments
We would like to thank Matthew Herman for his knowledge of, and thoughts on, the Bayesian search methodology. The continued (long-term) operation of the GPS stations in Central Sulawesi, Indonesia data has been cofacilitated by the EU-ASEAN SEAMERGES (2004–2006) and GEO2TECDI-1/2 projects (2009–2013). The GPS data acquisition and research were also partly funded by grants from the Dutch NWO User Support Programme Space Research (2007–2019). We would like to express our special thanks to the local staff of the Indonesian Meteorology, Climatology, and Geophysical Agency (BMKG) offices in Palu for providing their local micro-seismic data catalog. N. Nijholt was funded by the NWO ALW-GO/16-35 project. We would like to thank Lin Shen, Andy Hooper, and Taco Broerse for sharing their coseismic slip distribution that we displayed in Figure 2a (Shen et al., 2021). We would like to thank the Editor, Maureen Long, and are grateful to the Associated Editor, Attreyee Ghosh, an anonymous reviewer and Roland Bürgmann for their constructive comments.

References

Bacques, G., de Michele, M., Foumelis, M., Raucoules, D., Lemoine, A., & Briole, P. (2020). Sentinel optical and SAR data highlights multi-segment faulting during the 2018 Palu-Sulawesi earthquake (Mw 7.5). *Scientific Reports*, *10*, 9103. https://doi.org/10.1038/s41598-020-66032-7

Bacques, G., de Michele, M., Raucoules, D., Aochi, H., & Rolandone, F. (2018). Shallow deformation of the San Andreas fault 5 years following the 2004 Parkfield earthquake (Mw6) combining ERS2 and Envisat InSAR. *Scientific Reports*, *8*, 6032. https://doi.org/10.1038/s41598-018-24447-3

Bao, H., Ampuero, J.-P., Meng, L., Fielding, E. J., Liang, C., Milliner, C. W. D., et al. (2019). Early and persistent supershear rupture of the 2018 magnitude 7.5 Palu earthquake. *Nature Geoscience*, *12*, 200. https://doi.org/10.1038/s41561-018-0297-z

Bellier, O., Sébrier, M., Beaudouin, T., Villeneuve, M., Braucher, R., Bourles, D., et al. (2001). High slip rate for a low seismicity along the Palu-Koro active fault in central Sulawesi (Indonesia). *Terra Nova*, *13*(6), 463–470.

Bertiger, W., Desai, S. D., Haines, B., Harvey, N., Moore, A. W., Owen, S., & Weiss, J. P. (2010). Single receiver phase ambiguity resolution with GPS data. *Journal of Geodesy*, *84*, 327–337. https://doi.org/10.1007/s00190-010-0371-9

Biggs, J., Burgmann, R., Freymueller, J. T., Lu, Z., Parsons, B., Ryder, I., et al. (2009). The postseismic response to the 2002M7.9 Denali Fault earthquake: Constraints from InSAR 2003-2005. *Geophysical Journal International*, *176*(2), 353–367. https://doi.org/10.1111/j.1365-246X.2008.03932.x

Blewitt, G., & Lavallée, D. (2002). Effect of annual signals on geodetic velocity. *Journal of Geophysical Research*, *107*(B7), 2145–2156. https://doi.org/10.1029/2001JB000570

Bos, M. S., & Scherneck, H. G. (2014). *Onsala space observatory*. Retrieved from http://holt.oso.chalmers.se/loading

Bouchon, M., & Karabulut, H. (2008). The aftershock signature of supershear earthquakes. *Science*, *320*, 1323–1325. https://doi.org/10.1126/science.1155030

Bruhat, L. (2020). A physics-based approach of deep interseismic creep for viscoelastic strike-slip earthquake cycle models. *Geophysical Journal International*, *220*(1), 79–95. https://doi.org/10.1093/gji/ggz426

Bürgmann, R., Ergintav, S., Segall, P., Hearn, E., McClusky, S., Reilinger, R., et al. (2002). Time-dependent distributed afterslip on and deep below the Izmit earthquake rupture. *Bulletin of the Seismological Society of America*, *92*, 126–137. https://doi.org/10.1785/0120000833

Cipta, A., Robiana, R., Griffin, J. D., Horspool, N., Hidayati, S., & Cummins, P. R. (2017). A probabilistic seismic hazard assessment for Sulawesi, Indonesia. *Geological Society, London, Special Publications*, *441*(1), 133–152. https://doi.org/10.1144/sp441.6

Ding, K., Freymueller, J. T., Wang, Q., & Zou, R. (2015). Coseismic and Early Postseismic Deformation of the 5 January 2013 Mw 7.5 Craig Earthquake from Static and Kinematic GPS Solutions. *Bulletin of the Seismological Society of America*, *105*, 1153–1164. https://doi.org/10.1785/0120140172

Duputel, Z., Agram, P. S., Simons, M., Minson, S. E., & Beck, J. L. 2014). Accounting for prediction uncertainty when inferring subsurface fault slip. *Geophysical Journal International*, *197*(1), 464–482. https://doi.org/10.1093/gji/ggt517

Freed, A. M., Bürgmann, R., Calais, E., Freymueller, J., & Hreinsdóttir, S. (2006). Implications of deformation following the 2002 Denali, Alaska, earthquake for postseismic relaxation processes and lithospheric rheology. *Journal of Geophysical Research*, *111*, B01401. https://doi.org/10.1029/2005JB003894

GEER-team. (2019). *Geotechnical report on 2018 Palu-Donggala earthquake* (ISBN: 978-602-5489-19-8).

Hamilton, W. (1979). *Tectonics of the Indonesian region*. U.S. Geological Survey Professional Paper, IHUV, p. 345.

Hearn, E. H., Bürgmann, R., & Reilinger, R. E. (2002). Dynamics of Izmit earthquake postseismic deformation and loading of the Duzce earthquake hypocenter. *Bulletin of the Seismological Society of America*, *92*, 172–193. https://doi.org/10.1785/0120000832

Hearn, E. H., McClusky, S., Ergintav, S., & Reilinger, R. E. (2009). Izmit earthquake postseismic deformation and dynamics of the North Anatolian Fault Zone. *Journal of Geophysical Research*, *114*, B08405. https://doi.org/10.1029/2008JB006026

Herman, M. W., Furlong, K. P., & Govers, R. (2018). The accumulation of slip deficit in subduction zones in the absence of mechanical coupling: Implications for the behavior of megathrust earthquakes. *Journal of Geophysical Research: Solid Earth*, *123*, 8260–8278. https://doi.org/10.1029/2018JB016336

Herman, M. W., & Govers, R. (2020). Locating fully locked asperities along the South America subduction megathrust: A new physical inter-seismic inversion approach in a Bayesian framework. *Geochemistry, Geophysics, Geosystems*, *21*, e2020GC009063. https://doi.org/10.1029/2020GC009063

Jet Propulsion Laboratory. (2017). *GNSS-inferred positioning system and orbit analysis simulation software (GIPSY-OASIS)*. Retrieved from https://gipsy-oasis.jpl.nasa.gov

Johnson, K. M., Bürgmann, R., & Freymueller, J. T. (2009). Coupled afterslip and viscoelastic flow following the 2002 Denali Fault, Alaska earthquake. *Geophysical Journal International*, *176*, 670–682. https://doi.org/10.1111/j.1365-246X.2008.04029.x

Johnson, K. M., & Segall, P. (2004). Viscoelastic earthquake cycle models with deep stress-driven creep along the San Andreas fault system. *Journal of Geophysical Research*, *109*, B10403. https://doi.org/10.1029/2004JB003096

Katili, J. A. (1970). Large transcurrent faults in Southeast Asia with special reference to Indonesia. *Geologische Rundschau*, *59*(2), 581–600. https://doi.org/10.1007/bf01823809

Minson, S. E., Simons, M., & Beck, J. L. (2013). Bayesian inversion for finite fault earthquake source models I – Theory and algorithm. *Geophysical Journal International*, *194*, 1701–1726. https://doi.org/10.1093/gji/ggt180

Mustafar, M. A., Simons, W. J. F., Tongkul, F., Satirapod, C., Omar, K. M., & Visser, P. N. A. M. (2017). Quantifying deformation in North Borneo with GPS. *Journal of Geodesy*, *91*, 1241–1259. https://doi.org/10.1007/s00190-017-1024-z

Nur, A., & Mavko, G. (1974). Postseismic viscoelastic rebound. *Science*, *183*(4121), 204–206. https://doi.org/10.1126/science.183.4121.204

Okada, Y. (1992). Internal deformation due to shear and tensile faults in a half-space. *Bulletin of the Seismological Society of America*, *82*(2), 1018–1040.

Peltzer, G., Rosen, P., Rogez, F., & Hudnut, K. (1996). Postseismic rebound in fault step-overs caused by pore fluid flow. *Science*, *273*, 1202–1204. https://doi.org/10.1126/science.273.5279.1202

Prasetya, G. S., De Lange, W. P., & Healy, T. R. (2001). The Makassar Strait Tsunamigenic region, Indonesia. *Natural Hazards*, *24*(3), 295–307. https://doi.org/10.1023/A:1012297413280

Rebischung, P., & Schmid, R. (2016). *IGS14/igs14.atx: A new framework for the IGS products*. San Francisco, CA: AGU Fall Meeting.

Reilinger, R. E., Ergintav, S., Bürgmann, R., McClusky, S., Lenk, O., Barka, A., et al. (2000). Coseismic and postseismic fault slip for the 17 August 1999, M = 7.5, Izmit, Turkey earthquake. *Science*, *289*, 1519–1524. https://doi.org/10.1126/science.289.5484.1519

Rousset, B., Bürgmann, R., & Campillo, M. (2019). Slow slip events in the roots of the San Andreas fault. *Science Advances*, *5*, eaav3274. https://doi.org/10.1126/sciadv.aav3274

Shen, L., Broerse, D. B. T., Simons, W., Nijholt, N., Riva, R., & Hooper, A. (2021). *A co-seismic fault slip distribution for the Mw 7.5 2018 Palu earthquake*. 4TU.ResearchData. Dataset. https://doi.org/10.4121/14075894.v1

Simons, W. J. F., Riva, R. E. M., Pietrzak, J., Herman, M. W., Hooper, A. J., Vigny, C., et al. (2018). *Tsunami potential of the 2018 Sulawesi earthquake from GNSS constrained source mechanism*. AGU Fall Meeting Abstracts AGU, NH23F-3553.

Smith, S. W., & Wyss, M. (1968). Displacement on the San Andreas fault subsequent to the 1966 Parkfield earthquake. *Bulletin of the Seismological Society of America*, *58*, 1955–1973.

Socquet, A., Hollingsworth, J., Pathier, E., & Bouchon, M. (2019). Evidence of supershear during the 2018 magnitude 7.5 Palu earthquake from space geodesy. *Nature Geoscience*, *12*(3), 192. https://doi.org/10.1038/s41561-018-0296-0

Socquet, A., Simons, W., Vigny, C., McCaffrey, R., Subarya, C., Sarsito, D., et al. (2006). Microblock rotations and fault coupling in SE Asia triple junction (Sulawesi, Indonesia) from GPS and earthquake slip vector data. *Journal of Geophysical Research*, *111*, B08409. https://doi.org/10.1029/2005JB003963

Stevens, C., McCaffrey, R., Bock, Y., Genrich, J., Endang, Subarya, C., et al. 1999). Rapid rotations about a vertical axis in a collisional setting revealed by the Palu Fault, Sulawesi, Indonesia. *Geophysical Research Letters, 26*, 2677–2680.

Supendi, P., Nugraha, A. D., Widiyantoro, S., Pesicek, J. D., Thurber, C. H., Abdullah, C. I., et al. (2020). Relocated aftershocks and background seismicity in eastern Indonesia shed light on the 2018 Lombok and Palu earthquake sequences. *Geophysical Journal International*, *221*(3), 1845–1855. https://doi.org/10.1093/gji/ggaa118

Tarantola, A. (2005). *Inverse problem theory and methods for model parameter estimation*. SIAM.

Uchida, N., Kalafat, D., Pinar, A., & Yamamoto, Y. (2019). Repeating earthquakes and interplate coupling along the western part of the North Anatolian Fault. *Tectonophysics*, *769*, 228185. https://doi.org/10.1016/j.tecto.2019.228185

Vigny, C., Perfettini, H., Walpersdorf, A., Lemoine, A., Simons, W., van Loon, D., & Bock, Y. (2002). Migration of seismicity and earthquake interactions monitored by GPS in SE Asia triple junction: Sulawesi, Indonesia. *Journal of Geophysical Research*, *107*(B10), 2231. https://doi.org/10.1029/2001JB000377

Walpersdorf, A., Rangin, C., & Vigny, C. (1998a). GPS compared to long-term geologic motion of the north arm of Sulawesi. *Earth and Planetary Science Letters*, *159*(1–2), 47–55. https://doi.org/10.1016/s0012-821x(98)00056-9

Walpersdorf, A., Vigny, C., Subarya, C., & Manurung, P. (1998b). Monitoring of the Palu-Koro Fault (Sulawesi) by GPS. *Geophysical Research Letters*, *25*, 2313–2316.

Wang, K., Hu, Y., & He, J. (2012). Deformation cycles of subduction earthquakes in a viscoelastic Earth. *Nature*, *484*, 327–332. https://doi.org/10.1038/nature11032

Wang, L., Wang, R., Roth, F., Enescu, B., Hainzl, S., & Ergintav, S. (2009). Afterslip and viscoelastic relaxation following the 1999M7.4 İzmit earthquake from GPS measurements. *Geophysical Journal International*, *178*(3), 1220–1237. https://doi.org/10.1111/j.1365-246X.2009.04228.x

Wang, R., Lorenzo-Martín, F., & Roth, F. (2006). PSGRN/PSCMP – A new code for calculating co- and post-seismic deformation, geoid and gravity changes based on the viscoelastic-gravitational dislocation theory. *Computers and Geosciences*, *32*, 527–541. https://doi.org/10.1016/j.cageo.2005.08.006

Watkinson, I. M., & Hall, R. (2017). Fault systems of the eastern Indonesian triple junction: Evaluation of quaternary activity and implications for seismic hazards. *Geological Society, London, Special Publications*, *441*(1), 71–120. https://doi.org/10.1144/sp441.8

Watkinson, I. M., & Hall, R. (2019). Impact of communal irrigation on the 2018 Palu earthquake-triggered landslides. *Nature Geoscience*, *12*, 940–945. https://doi.org/10.1038/s41561-019-0448-x

Wilson, P., Rais, J., Reigber, C., Reinhart, E., Ambrosius, B. A. C., Le Pichon, X., et al. (1998). Study provides data on active plate tectonics in Southeast Asia Region. *Eos, Transactions American Geophysical Union*, *79*, 545.

Wimpenny, S., Copley, A., & Ingleby, T. (2017). Fault mechanics and post-seismic deformation at Bam, SE Iran. *Geophysical Journal International*, *209*, 1018–1035. https://doi.org/10.1093/gji/ggx065

Wright, T. J., Elliott, J. R., Wang, H., & Ryder, I. (2013). Earthquake cycle deformation and the Moho: Implications for the rheology of continental lithosphere. *Tectonophysics*, *609*, 504–523. https://doi.org/10.1016/j.tecto.2013.07.029

Wright, T. J., Lu, Z., & Wicks, C. (2004). Constraining the Slip Distribution and Fault Geometry of the Mw 7.9, 3 November 2002, Denali Fault Earthquake with Interferometric Synthetic Aperture Radar and Global Positioning System Data. *Bulletin of the Seismological Society of America*, *94*(6B), S175–S189. https://doi.org/10.1785/0120040623

Yue, H., Lay, T., Freymueller, J. T., Ding, K., Rivera, L., Ruppert, N. A., & Koper, K. D. (2013). Supershear rupture of the 5 January 2013 Craig, Alaska (Mw 7.5) earthquake. *Journal of Geophysical Research: Solid Earth*, *118*, 5903–5919. https://doi.org/10.1002/2013JB010594

Zumberge, J. F., Heflin, M. B., Jefferson, D. C., Watkins, M. M., & Webb, F. H. (1997). Precise point positioning for the efficient and robust analysis of GPS data from large networks. *Journal of Geophysical Research*, *102*, 5005–5017.

Reference From the Supporting Information

Altamimi, Z., Rebischung, P., Métivier, L., & Collilieux, X. (2016). ITRF2014: A new release of the International Terrestrial Reference Frame modeling non-linear station motions. *Journal of Geophysical Research: Solid Earth*, *121*(8), 6109–6131. https://doi.org/10.1002/2016JB013098